

Charge and Spin Transport at the Quantum Hall Edge of Graphene

Dmitry A. Abanin, Patrick A. Lee, Leonid S. Levitov

Department of Physics, Massachusetts Institute of Technology, 77 Massachusetts Ave, Cambridge, MA 02139

Landau level bending near the edge of graphene, described using 2d Dirac equation, provides a microscopic framework for understanding the quantum Hall Effect (QHE) in this material. We review properties of the QHE edge states in graphene, with emphasis on the novel phenomena that arise due to Dirac character of electronic states. A method of mapping out the dispersion of edge states using scanning tunneling probes is proposed. The Zeeman splitting of Landau levels is shown to create a particularly interesting situation around the Dirac point, where it gives rise to counter-circulating modes with opposite spin. These chiral spin modes lead to a rich variety of spin transport phenomena, including spin Hall effect, spin filtering and injection, and electric detection of spin current. The estimated Zeeman spin gap, enhanced by exchange, of a few hundred Kelvin, makes graphene an attractive system for spintronics. Comparison to recent transport measurements near $\nu = 0$ is presented.

INTRODUCTION

Isolation and gating [1] of graphene, a monolayer of graphite, has enabled the observation of interesting transport effects, resulting from Dirac fermion-like character of excitations. In particular, graphene hosts an integer quantum Hall effect (QHE) with unusual plateau structure [2, 3]. It was found that the QHE plateaus in monolayer are arranged symmetrically around the neutrality point, occurring at filling factors which are half-integer multiples of four, which is the combined spin and valley degeneracy of graphite. This form of QHE came to be known as the anomalous or half-integer QHE.

The simplest framework allowing to understand this behavior of QHE is provided by the structure of Landau levels (LL) of a 2d massless Dirac equation [28] which has the particle-hole symmetric spectrum

$$E_n = \pm \varepsilon_0 \sqrt{|n|}, \quad \varepsilon_0 = \hbar v_0 \sqrt{2eB/\hbar c} \quad (1)$$

with the sign plus for positive n , and minus for negative n . Here B is the magnetic field and $v_0 \approx 8 \times 10^7$ cm/s is the velocity at the graphite Dirac point K or K' . Due to spin and valley degeneracy (we shall discuss the role of Zeeman splitting below), each of the levels (1) contributes a step of $4e^2/h$ to the quantized Hall conductivity. The particle-hole symmetry $\varepsilon \rightarrow -\varepsilon$ of the spectrum (1), with the $n = 0$ level positioned at $\varepsilon = 0$, suggests that the QHE plateaus must occur at $\nu = \pm 2(2n + 1) = \pm 2, \pm 6, \pm 10, \dots$, which is indeed what is observed in experiment [2, 3]. The anomalous QHE in graphene can be understood in a more fundamental way in terms of a quantum anomaly of the zeroth Landau

level [4]. The special character of the monolayer spectrum (1) is underscored by the difference between the QHE properties observed in graphene monolayer and bilayer systems [5].

One of the most dramatic consequences of the Dirac LL spectrum (1) is the appearance of the new energy scale ε_0 . The square root dependence $\varepsilon_0 \propto \sqrt{B}$ leads to a much larger level spacing than that for electrons with the quadratic dispersion conventional for semiconductors. For typical magnetic field of 10 T, the separation of the lowest LL ($n = 0, 1$) is quite large, $\Delta E = \varepsilon_0 \approx 1000$ K, which enables QHE to persist up to room temperature [6].

To gain insight into the microscopic origin of the anomalous QHE, it is useful to develop the edge-states approach, which provides an intuitive and simple picture of the conventional QHE [7]. The edge states for graphene were studied using a numerical solution of the tight-binding model [8] and also with the help of the Dirac equation [9, 10]. It was found that the energy levels (1), valley-degenerate in the graphene bulk, are split near the edge due to valley mixing at the boundary. Interestingly, it turns out that the structure and dispersion of the edge states depend on particular crystallographic orientation of the edge. For the so-called armchair edge, a simple particle-hole symmetric splitting was found [9]. Particle-like and hole-like states have different sign of energy dispersion, giving rise to counter-propagating modes with opposite chirality. A somewhat more complicated situation occurs near the zigzag edge, where dispersing edge states coexist with an additional dispersionless surface state [8]. Despite these differences, the armchair, zigzag and other edges have same numbers of dispersing edge states of both chiralities. As we discuss below in Sec.II, this ensures the universal half-integer character of QHE in graphene.

One unique aspect of QHE in graphene is that its electronic states, owing to the monolayer character of this material, are fully exposed and, similar to the surface states of 3d materials, can be investigated by scanning

[28] The result (1) follows from the well-known representation of the Schrödinger-Pauli Hamiltonian as a square of a massless Dirac Hamiltonian, $H_{\text{SP}} = \frac{1}{2m} (\sigma^i (p_i - \frac{e}{c} A_i))^2$. The Dirac spectrum (1) is then obtained by taking a square root of the nonrelativistic Landau level spectrum.

tunneling microscopy (STM) probes with atomic resolution. Moreover, some useful information can even be obtained by imaging the top layer of 3d graphite, as demonstrated by recent STM studies of Dirac Landau levels [11, 12] and of electron states near atomically thin edges [13, 14]. In Sec.II we discuss new possibilities for scanning experiments that arise in graphene. The characteristic spatial scale of the states in a Landau level, given by the magnetic length $\ell_B = (\hbar c/eB)^{1/2}$, is about 8 nm for the field of 10 T. Being large compared to the STM spatial resolution, it allows to image individual electronic states with sub- ℓ_B resolution and, in particular, to study Landau level bending near graphene edge. This bending in fact mimics the edge states momentum dispersion, due to the position-momentum duality of the Landau levels. As we shall see, the STM technique has sufficient resolution to map out the dispersion of QHE edge states.

Another novel feature of graphene is the simultaneous presence of the QHE edge modes of opposite chiralities, propagating in the opposite directions. Being particle-like and hole-like, they occur at the energies $\varepsilon > 0$ and $\varepsilon < 0$, respectively. For electron density detuned from the neutrality point, $\nu = 0$, only one of the chiralities contributes to transport. However, as we shall see, near $\nu = 0$ the states of both chiralities can participate in transport, leading to rather unusual transport properties. In particular, in the presence of Zeeman spin splitting of Landau levels, the $\nu = 0$ state features an energy gap in the bulk and, simultaneously, a pair of edge states of opposite chirality and opposite spin polarization [9, 15]. These states carry spin-up and spin-down electrons in the opposite directions along graphene edge, exhibiting quantized spin Hall effect but no charge Hall effect, owing to the particle-hole symmetry at $\nu = 0$. As we discuss in Sec.III, these spin-polarized chiral edge states exhibit interesting spin transport phenomena, such as spin filtering and spin injection, whereas the spin Hall effect provides a natural tool for the detection of spin current.

Interestingly, the counter-propagating edge states manifest themselves directly in charge transport. As we discuss in Sec.IV, near $\nu = 0$ longitudinal resistivity remains finite, $\rho_{xx} \gtrsim h/e^2$, while the Hall effect, which is absent at the particle-hole symmetry point $\nu = 0$, appears at nonzero ν due to conductivity in the bulk. This leads to Hall resistance ρ_{xy} changing sign at $\nu = 0$ without exhibiting a clear plateau. The bulk conductivity short-circuits the edge transport and suppresses longitudinal resistivity, leading to a prominent peak in ρ_{xx} near $\nu = 0$ and a plateau in σ_{xy} . These predictions, as well as the behavior of resistance fluctuations, which are enhanced near zero ν , are in agreement with experiment [16, 17].

Looking beyond graphene, interesting massless Dirac fermion states have been predicted a while ago [18] at interfaces of narrow-gapped HgTe and PbTe semiconductors. In Ref.[18], which anticipated many of the features

of electronic states in graphene, 2d Dirac states occur in a band-inverted heterojunction plane due to spin orbit interaction in 3d bulk, in the absence of magnetic field.

We note also that there have been interesting predictions of quantized spin Hall effect in certain 2d insulators [19, 20]. In particular, the proposal of Ref.[20] can be viewed as a 2d version of the 3d situation discussed in Ref.[18]. In these schemes an energy gap forms in the bulk due to spin-orbit even in the absence of magnetic field, similar to Ref.[18]. At the same time, counter-propagating modes carrying opposite spins appear on the edge, which are responsible for the quantized spin Hall current. As was emphasized in Ref.[22], there are general symmetry requirements, rooted in the time-reversal symmetry, protecting counter-propagating gapless excitations at an insulator boundary. In particular, certain Z_2 invariants must exist, which are realized as spin σ_z component in the case of graphene [9, 19], and were linked to supersymmetry for heterojunction systems [18].

We note that the nature of the edge states of Refs.[19, 20] is essentially identical to ours. The only difference, apart from different size of the energy gap, is that Rashba spin-orbit may cause backscattering in our case (see Sec.III) but not in the situation of Refs.[18, 19, 20], while magnetic impurities will cause backscattering in both cases. In particular, our discussion in Sec.IV of ρ_{xx} and ρ_{xy} and our proposals to operate and detect spin current can serve as diagnostic tools should these schemes become realized experimentally.

The rest of the paper is organized as follows. In Sec.II we introduce the edge states using the Dirac equation framework. We focus on the two main edge types, armchair and zigzag, however we emphasize the generic aspects that are applicable to other edges. Then we discuss the anomalous QH effect and the possibility of imaging the edge states with scanning tunneling probes. In Sec.III we focus on spin-polarized chiral edge states and related spin transport phenomena. We also comment on spin relaxation mechanisms and present estimates of the spin relaxation time. In Sec.IV we introduce a transport model which accounts for both edge and bulk transport. This allows us to connect the chiral spin-polarized edge picture with recent transport measurements near the neutrality point [16, 17].

II. DIRAC QHE EDGE STATES

Here we analyze electron states near zigzag and armchair edges (Fig.1a), the two most common graphene edge types, using massless Dirac model [21]. This exercise, which amounts to setting the boundary conditions for the Dirac spinor and solving an appropriate 1d eigenvalue problem, provides a fully microscopic picture of graphene QHE. Below we use this approach to illustrate the interplay between the QHE edge states and surface

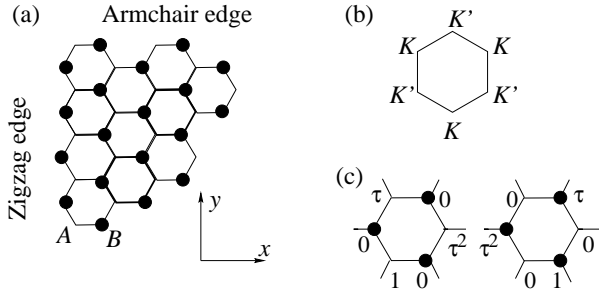


FIG. 1: (a) Graphene lattice with armchair and zigzag edges. Sublattices A and B are marked. (b) Graphene hexagonal Brillouin zone with Dirac valleys K and K' . (c) The two linearly independent zero-energy Bloch functions for the K valley used in (2), where $\tau = e^{2\pi i/3}$. For the K' point, the zero-energy Bloch functions are obtained from those shown by complex conjugation.

states for the zigzag edge, and discuss the possibility of imaging the edge states with scanning tunneling probes.

Let us first recall how low-energy graphene excitations are obtained in the tight-binding model[21] near the Dirac valleys K and K' , located at the two non-equivalent Brillouin zone corners (see Fig.1(b)). There are two linearly independent zero-energy Bloch functions for each of the points K , K' , each residing only on one sublattice (A or B) and vanishing on the other sublattice. Our choice of Bloch functions for the K valley is shown in Fig.1(c). The Bloch functions for the valleys K and K' are related by complex conjugation.

The wave function of low-lying excitations near K and K' , is written as a superposition of these four zero-energy Bloch functions multiplied by slowly varying envelope functions u_K , v_K , $-u_{K'}$, $-v_{K'}$, with u and v being the wave function amplitudes on the sublattice A and B . (Our choice of the signs for the K' valley is convenient for treating an armchair boundary, as we shall see below.) The envelope functions u_K , v_K , and $u_{K'}$, $v_{K'}$ describe excitations near K and K' , respectively. The effective low-energy Hamiltonian, obtained by keeping only lowest-order gradients of u and v , takes the massless Dirac form [29]:

$$H_K = iv_0 \begin{bmatrix} 0 & \tilde{p}_+ \\ -\tilde{p}_- & 0 \end{bmatrix}, \quad H_{K'} = iv_0 \begin{bmatrix} 0 & \tilde{p}_- \\ -\tilde{p}_+ & 0 \end{bmatrix}, \quad (2)$$

where $\tilde{p}_\pm = \tilde{p}_x \pm i\tilde{p}_y$, $\tilde{p}_\mu = p_\mu - (e/c)A_\mu$.

Landau levels in an external B -field, described with the gauge $A_x = -By$, $A_y = 0$, can be obtained for the

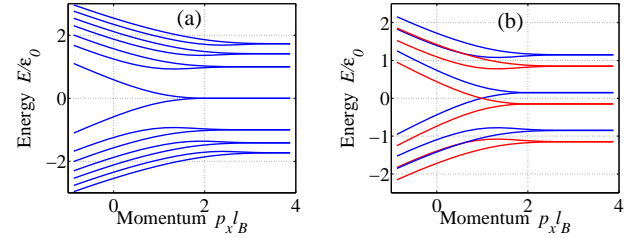


FIG. 2: (a) Electron energy spectrum near the armchair boundary obtained from the Dirac model, Eq.(2). The boundary condition, Eq.(7), lifts the K , K' degeneracy, forming particle-like and hole-like counter-propagating edge modes. The odd integer numbers of the modes yields the ‘half-integer’ QHE. (b) Spin-split graphene edge states, propagating in opposite directions at zero energy: the blue (red) curves represent the spin up (spin down) states.

states with the x dependence $e^{ip_x x}$ from 1d Hamiltonians

$$H_{K,K'} = \frac{i\varepsilon_0}{\sqrt{2}} \begin{bmatrix} 0 & \pm\partial_y + (y - y_*) \\ \pm\partial_y - (y - y_*) & 0 \end{bmatrix}, \quad (3)$$

where $\varepsilon_0 = \hbar v_0 (2eB/\hbar c)^{1/2}$ and $y_* = -p_x$. Here y and p_x are measured in the units of ℓ_B and \hbar/ℓ_B , respectively. The spectrum of $H_{K,K'}$, Eq.(3), yields the Dirac Landau levels, Eq.(1), where the eigenstates for the two valleys $K(K')$ are given by

$$(u_{K,n}, v_{K,n}) = A(c_n \varphi_{n-1}(y - y_*), \varphi_n(y - y_*)), \quad (4)$$

$$(u_{K',n}, v_{K',n}) = A(\varphi_n(y - y_*), c_n \varphi_{n-1}(y - y_*)). \quad (5)$$

Here $\varphi_n(z)$ are the eigenfunctions of the magnetic oscillator, $n = 0, 1, \dots$, the normalization factor A equals 1 for $n = 0$ and $1/\sqrt{2}$ for $n \neq 0$, with $c_0 = 0$ and $c_{n \neq 0} = 1$. Note that zeroth LL states reside solely on B sublattice for valley K and on A sublattice for valley K' [30].

We now analyze how LL spectrum is modified near the armchair edge. We consider graphene sheet in the halfplane $y < 0$ with an armchair edge parallel to the x axis (see Fig.1(a)). Energy levels near the edge are determined from the Dirac eigenvalue equations $E\psi = H_{K,K'}\psi$, where $\psi = (u, v)$, and $H_{K,K'}$ are given by Eq.(3). To analyze this eigenvalue problem, we exclude v components and consider eigenvalue equations with spectral parameter $\lambda = (E/\varepsilon_0)^2$ for u components:

$$\frac{1}{2}(-\partial_y^2 + (y - y_*)^2 + 1) u_K = \lambda u_K, \quad \frac{1}{2}(-\partial_y^2 + (y - y_*)^2 - 1) u_{K'} = \lambda u_{K'}, \quad (6)$$

The boundary conditions for Eqs.(6) can be obtained from the tight-binding model, which is valid up to the

[29] We note that the Hamiltonian used in our paper [9] is related to the Hamiltonian (2) by variable transformation $u_{K,K'} \rightarrow u_{K,K'}$, $v_{K,K'} \rightarrow -iv_{K,K'}$.

[30] This property is specific for the zeroth LL, making the splitting of the $n = 0$ LL due to Coulomb interaction distinctly different from that of other LLs (see [27, 28]).

very last row near $y = 0$, by setting the wave function equal zero at the boundary. Since the armchair edge has lattice sites of both A and B type (see Fig.1(a)), the wave function on both sublattices should vanish at the edge. In terms of the envelope functions $u_{K,K'}$, $v_{K,K'}$, taken at $y = 0$, this condition translates into

$$u_K = u_{K'}, \quad v_K = v_{K'}. \quad (7)$$

We obtain a pair of differential equations (6) on the semi-axis $y < 0$, coupled at the boundary via Eq.(7). To simplify this problem, let us map Eq.(6) for $u_{K'}$ onto the positive semi-axis $y > 0$, by $u_{K'}(y) \rightarrow u_{K'}(-y)$, while keeping u_K on the negative semi-axis $y < 0$, and treat it as an eigenvalue problem in the domain $-\infty < y < \infty$ with the wavefunction given by u_K at negative y and by $u_{K'}$ at positive y . The first boundary condition, Eq.(7), then means that the wavefunction is continuous at $y = 0$, while the second condition implies continuity of the derivative $\partial u / \partial y$. (This can be seen by expressing $v_{K,K'}$ in terms of $u_{K,K'}$ using Eqs.(3).) Thus we obtain a 1d Schrödinger problem in the potential [9]

$$V(y) = \frac{1}{2}(|y| + y_*)^2 - \frac{1}{2}\text{sgn}(y), \quad (8)$$

defined on the entire y axis. After finding the spectrum $\lambda(y_*)$ numerically, we obtain the energy levels of the Dirac fermions as

$$E(p_x) = \pm \varepsilon_0 \sqrt{\lambda(y_*)}, \quad y_* = -p_x, \quad (9)$$

whereby the particle-hole symmetry is restored due to the two possible signs of $E(p_x)$. The dispersion (9) is illustrated in Fig.2a. We note that the LL double valley degeneracy in the bulk is lifted at the boundary.

The particle-hole symmetric edge states spectrum in Fig.2a instantly explains the “half-integer” Hall quantization in graphene. Indeed, for any electron density with integer ν in the bulk there is an odd number of the edge modes crossing the Fermi level, which means that the Hall conductivity is quantized as $\sigma_{xy} = 2(2n+1)e^2/h$, where the factor two accounts for spin degeneracy.

Spin degeneracy of the Landau levels is lifted by the Zeeman interaction, which is substantial in graphene,

$$E_Z = g\mu_B B \approx 50 \text{ K}, \quad g \approx 2, \quad (10)$$

for $B = 30 \text{ T}$ (compare to $g \sim 0.1$ in GaAs quantum wells). Zeeman-split edge states, depicted in Fig.2b, have interesting characteristics for electron density near neutrality, $\nu = 0$. At this density the state in the bulk is spin-polarized, with the Zeeman gap further enhanced by exchange (see below). The two branches of counter-propagating edge states near $\varepsilon = 0$, carrying opposite spin, have interesting properties that will be discussed in more detail in Sec.III.

We now analyze the *zigzag* edge, which even at $B = 0$ hosts a band of dispersionless zero-energy states bound

to the edge [23]. We shall refer to these states as surface states, to distinguish them from the dispersing QHE edge states. As we shall see, the surface states contribute to the splitting of $n = 0$ LL near the zigzag edge, in agreement with the tight-binding calculations [8].

We consider graphene sheet in the half-plane $x > 0$, with its first row consisting of B atoms (see Fig.1a). For the states with the y dependence $e^{ip_y y}$, with $A_x = 0$, $A_y = Bx$, from (2) we obtain 1d Hamiltonians

$$H_{K,K'} = \frac{\varepsilon_0}{\sqrt{2}} \begin{bmatrix} 0 & \partial_x \pm (x - x_*) \\ -\partial_x \pm (x - x_*) & 0 \end{bmatrix}, \quad (11)$$

where $x_* = p_y$. Similarly to the armchair case, the spectrum can be found from the eigenvalue equation $E\psi = H_{K,K'}\psi$, where $\psi = (u, v)$, which should be supplemented with the boundary conditions. For our zigzag edge the wavefunction must vanish on all A sites at $x = 0$. For that both envelope functions $u_K, u_{K'}$ have to vanish at the boundary,

$$u_K = 0, \quad u_{K'} = 0. \quad (12)$$

Excluding v components, we obtain two separate eigenvalue problems for the spectral parameter $\lambda = (E/\varepsilon_0)^2$,

$$\begin{aligned} \frac{1}{2}(-\partial_x^2 + (x - x_*)^2 + 1) u_K &= \lambda u_K, \\ \frac{1}{2}(-\partial_x^2 + (x - x_*)^2 - 1) u_{K'} &= \lambda u_{K'}, \end{aligned} \quad (13)$$

where both u_K and $u_{K'}$ satisfy the hard wall boundary conditions (12). The amplitudes $v_{K,K'}$ on the B sublattice can be expressed via amplitudes $u_{K,K'}$ on the A sublattice and eigenenergy E ,

$$\begin{aligned} v_K &= (\varepsilon_0/\sqrt{2}E)(-\partial_x + (x - x_*)) u_K, \\ v_{K'} &= (\varepsilon_0/\sqrt{2}E)(-\partial_x - (x - x_*)) u_{K'}. \end{aligned} \quad (14)$$

The eigenvalue problems (13) with the hard-wall boundary conditions (12) are familiar from the theory of edge states in the conventional QHE [7], and their spectrum $\lambda(x_*)$ can be found numerically. The Dirac fermion energy dispersion $E(p_y) = \pm \varepsilon_0 \sqrt{\lambda(x_*)}$ is shown in Fig.3.

The behavior of $n \neq 0$ LL's is similar to the armchair case: there are two branches of the edge states, one for each valley, degenerate in the bulk, $x_* \gg 1$, which split near the edge. The zeroth LL, however, coexists with the surface state, which makes its behavior rather peculiar and different for the two valleys.

In the K valley, which we discuss first, the zeroth LL K states reside solely on the B sublattice, see Eq.(4), and therefore automatically satisfy the boundary condition $u_K = 0$. Thus there are zero-energy states for arbitrary values of x_* , of the form $\varphi_0(x - x_*) \propto e^{-(x-x_*)^2/2}$. Let us consider the states with x_* far outside the graphene half-plane, $x_* \ll -1$. Not too far from the boundary, such states can be approximated by an exponential

$$v_K(0 < x \lesssim |x_*|) \propto e^{-|x_*|x}, \quad u_K(x) = 0. \quad (15)$$

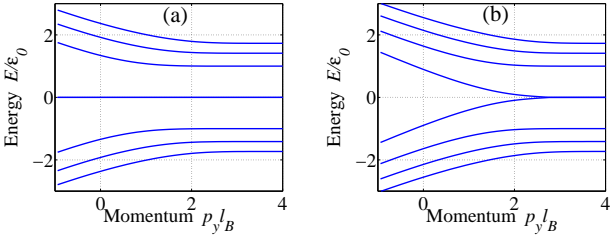


FIG. 3: Electron energy dispersion for the zigzag boundary obtained from the Dirac model, Eq.(2), (12). (a) Spectrum for the K valley. The zeroth LL morphs into dispersionless surface mode[23] near the edge. (b) Spectrum for the K' valley. The zeroth LL mixes with the surface mode, giving rise to two branches of dispersing QHE edge states.

which is identical to surface state wave function [23]. Thus the zeroth LL for valley K near the edge transforms into the surface mode. Being dispersionless, this mode does not contribute to the edge transport. The edge state spectrum for the valley K is displayed in Fig.3a.

Now let us consider the zeroth LL for the valley K' . For $x_* \gg 1$, we approximate the ground state of the oscillator (13) with the hard-wall boundary condition as

$$u_{K'}(x) = \psi_{x_*}(x) \approx \varphi_0(x - x_*) - \varphi_0(x + x_*). \quad (16)$$

The ground state energy $\lambda_0(x_*)$ is then approximated by

$$\lambda_0(x_*) \approx \langle h \rangle, \quad (17)$$

where $h = \frac{1}{2}(-\partial_x^2 + (x - x_*)^2 - 1)$ is the effective Hamiltonian for $u_{K'}$ component, Eq.(13), and $\langle \dots \rangle$ denotes averaging over the normalized wave function (16).

Evaluating $\langle h \rangle$ for $x_* \gg 1$, when the state (16) has unit norm with exponential accuracy, we obtain

$$\lambda_0(x_*) \approx x_* \pi^{-1/2} e^{-x_*^2}. \quad (18)$$

From the relation $E = \pm \varepsilon_0 \sqrt{\lambda}$, we find the energies for the two branches of dispersing edge states

$$E_{\pm}(x_*) \approx \pm (2x_*)^{1/2} \pi^{-1/4} e^{-x_*^2/2} \varepsilon_0. \quad (19)$$

Plugging this expression in Eq.(14), we obtain the wave function on B sublattice for these two branches,

$$v_{K'} = \pm x_*^{1/2} e^{-x_* x}. \quad (20)$$

which is again the surface state wave function (compare to Eq.(15)). We therefore conclude that for the K' valley the zeroth Landau level and the surface state mix giving rise to two dispersing edge modes. This is in agreement with the spectrum displayed in Fig.3b. We see that, although the Dirac model is applicable only in a small part of the Brillouin zone, near points K and K' , it provides a description of the states at the zigzag edge, including

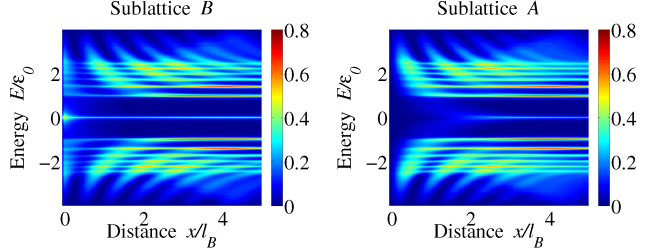


FIG. 4: Position-dependent tunneling spectroscopy of graphene near the zigzag edge for sublattices A and B . Due to the momentum-position duality, the dependence of LDOS, Eqs.(21), on the distance to the edge x mimics the momentum dispersion of the edge states. Note the difference of the spectra for the two sublattices near the edge and presence of surface state for sublattice B .

the surface state, which is in agreement with the results of the tight-binding model of Ref.[8]. The surface mode in the vicinity of K and K' is given by Eqs.(15),(20).

Interestingly, the A and B sites contribute equally to the splitting of the zeroth LL, $\int_{x>0} |u_{K'}|^2 dx = \int_{x>0} |v_{K'}|^2 dx$. This is somewhat counterintuitive, since this LL is solely on the sublattice A in the bulk, while the surface mode is solely on the sublattice B . This equal participation property can be understood as follows. The spinor states $(u_{K'}, \pm v_{K'})$ with $u_{K'}$, $v_{K'}$ given by Eqs.(16),(20), are eigenstates of the Dirac Hamiltonian with the boundary condition (12), with the energies $\pm E$. Thus these states are orthogonal, which implies that the integrals of $|u_{K'}|^2$ and $|v_{K'}|^2$ are equal. We further note that the integral of the square of the B component of our edge state wave function (20) over $x > 0$ indeed equals one, in agreement with our choice of normalization on the A sublattice in Eq.(16).

To sum up, for the zigzag edge, the zeroth LL gives rise to two dispersing edge states for one of the valleys, while for the other valley the zeroth LL morphs into the dispersionless surface mode which does not contribute to the edge current. Therefore, despite the presence of the surface mode, the number of dispersing QHE edge states with $\varepsilon > 0$ and $\varepsilon < 0$ for the zigzag boundary is the same as for the armchair boundary, giving rise to “half-integer” quantization of Hall current.

Finally, we briefly discuss how the edge states in graphene can be investigated using the STM technique [11, 12, 13, 14]. Due to the Landau level momentum-position duality relation, $p_y = (\hbar/\ell_B^2)x_*$, the edge state momentum dispersion shown in Figs.2,3 translates into the excitation energy dependence on the distance from the edge. The characteristic scale for the latter is set by the magnetic length ℓ_B , which for typical fields is about 50-80 times greater than the spatial resolution of STM instruments on graphite surface. This makes STM technique particularly convenient for this kind of

studies.

A link between the edge states dispersion and the position-dependent tunneling spectroscopy can be established as follows. We shall use the solutions for the edge state wave function given above to calculate the local density of states (LDOS) near the zigzag edge (other edge types can be dealt with similarly). For each of the graphene sublattices LDOS is given by

$$\begin{aligned}\rho_A(E, x) &= \sum_{\alpha} |u_{\alpha}(x)|^2 \delta(E - E_{\alpha}), \\ \rho_B(E, x) &= \sum_{\alpha} |v_{\alpha}(x)|^2 \delta(E - E_{\alpha}),\end{aligned}\quad (21)$$

where x is the distance from the edge, and α denotes the set of eigenstates of the K and K' Hamiltonians (11) with the hard-wall boundary condition (12).

Using the eigenfunctions $u_{\alpha}(x), v_{\alpha}(x)$ and the energies E_{α} found from Eqs.(13),(14) as discussed above, we obtain LDOS for the A and B sublattices which is displayed in Fig.4. We see that the position-independent Landau level bands, dominating LDOS far from the edge, bend away from $\epsilon = 0$ near the edge. This bending mimics the edge states momentum dispersion shown in Fig.3. Note, however, that LDOS is nonzero only for $x > 0$, whereas the edge state momentum p_y can be both positive and negative. The spatial width of the bending bands is determined by the width of the eigenfunctions $u_{\alpha}(x), v_{\alpha}(x)$, which is of the magnetic length scale.

III. SPIN-POLARIZED CHIRAL EDGE STATES AND SPIN TRANSPORT.

As we noted above, at the neutrality point $\nu = 0$ graphene hosts gapless spin-polarized edge states (see Fig.2(b)). The Zeeman energy gap in the bulk, Eq.(10), is enhanced by the Coulomb interaction. A Hartree-Fock estimate of this enhancement [9] gives

$$\Delta = \frac{\pi^{1/2} e^2}{2\kappa\hbar v_0} (1 - \alpha) \epsilon_0 \approx 0.456 \cdot (1 - \alpha) \epsilon_0, \quad (22)$$

where $\kappa = 1 + \pi e^2 / 2\hbar v_0 \approx 5.24$ is RPA screening function, and the parameter $0 < \alpha < 1$ describes relative strength of Coulomb and exchange correlations. Assuming $\alpha = 0$, i.e. ignoring correlations of electrons with opposite spin, we obtain a spin gap $\Delta \sim 800$ K for $B = 30$ T. Taking into account the substrate dielectric constant, $e^2 \rightarrow \frac{2}{\epsilon+1} e^2$, changes the result only slightly ($\frac{2}{\epsilon+1} = 0.36$ for SiO_2). This approximation, while pointing at a correct order of magnitude of a few hundred Kelvin, probably somewhat overestimates the spin gap since it ignores correlations and disorder effects.

The chiral spin-polarized edge states offer a unique setting to study spin transport. In particular, the spin-split state $\nu = 0$ may be used to generate and detect spin-polarized currents. This spin transport regime seems attractive due to the large bulk gap and high stability of

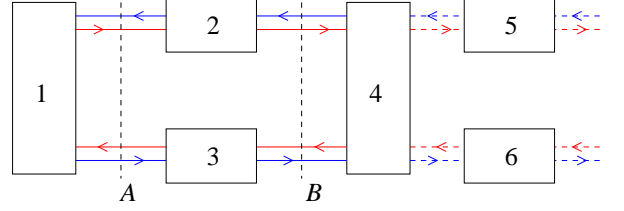


FIG. 5: A Hall bar at $\nu = 0$ can be used to generate and detect spin currents. Blue and red lines represent edge currents with up and down spins. Contacts 1 and 4 are source and drain, which may be used to inject spin polarized current. Contacts 2, 3 are voltage probes with full spin mixing. The measured Hall voltage is directly related to spin current flowing in the system. An asymmetry between the upper and lower edges, e.g., introduced by removing voltage probe 3 or by gating, creates spin filtering effect: an unpolarized current injected from source 1 induces a spin-polarized current flowing into drain 4. Hall probes 5 and 6 downstream can serve as detectors of spin currents.

the edge states. Moreover, increased quality of samples should allow existence of spin polarized edge states even at relatively low magnetic fields.

Since the purpose of this section is mostly illustrative, we will keep our discussion as simple as possible. In particular, we shall ignore transport in the bulk, leaving the discussion of its role for Sec.IV. We also first neglect spin flip backscattering between edge states within one edge. Estimates of the spin flip rate wil be given below, Eq.(24). A general approach, based on the Landauer-Büttiker formalism [24], which can be used to calculate spin and charge currents at the edge for any configuration of current and voltage leads, was presented in Ref.[9].

In this approach, transport is described by a scattering matrix [24], with the edge states playing the role of scattering channels, and the reservoirs supplying in-states and absorbing out-states. Current in each mode is described by the relation $I_{\uparrow(\downarrow)} = \frac{e^2}{h} \varphi_{\uparrow(\downarrow)}$, where $\varphi_{\uparrow(\downarrow)}$ is the reservoir chemical potential for given spin projection. We consider the Hall bar geometry with four contacts 1-4 (see Fig.5), where the contacts 1 and 4 serve as current source and drain. For these two contacts we do not assume spin mixing, so that the injected and drained current may be spin polarized. The contacts 2, 3 are voltage probes, which means that they do not drain current from the system. Furthermore, we assume that the probes provide full spin mixing, i.e. chemical potentials of outgoing spin-up and spin-down electrons are equal.

The simplest situation arises when unpolarized current is injected through contact 1. Then the up- and down-spins spatially separate in a symmetric way, flowing along the opposite edges of the bar. This can be interpreted as circulating spin current, and described as spin-Hall effect with quantized spin conductance $\sigma_{xy}^{(\text{spin})} = e^2/h$. No electric voltage will be induced between the voltage probes 2, 3 in this case (zero charge-Hall effect).

This device can be used as a detector of spin polarized current, made possible by the reciprocal of the spin Hall effect, in which the electric Hall voltage is directly related to spin rather than charge current. Suppose the up-spin and down-spin electrons, injected through contact 1, have unequal chemical potentials, $\varphi_\uparrow \neq \varphi_\downarrow$. Then the currents flowing into the probes 2 and 3, $I_{\uparrow(\downarrow)} = \frac{e^2}{h}\varphi_{\uparrow(\downarrow)}$, after equilibration and spin mixing in the probes, induce voltages $V_{2(3)} = \varphi_{\uparrow(\downarrow)}/2$. The resulting Hall voltage $V_{xy} = (\varphi_\downarrow - \varphi_\uparrow)/2$ is directly proportional to *spin current*. At the same time, an unpolarized current (for which $\varphi_\downarrow = \varphi_\uparrow$) flows symmetrically in the upper and lower edges without generating Hall voltage.

Spin transport at $\nu = 0$ also allows to realize spin filter. Suppose that the upper and lower edges of the device in Fig.5 are made asymmetric, which can be achieved, for example, simply by removing probe 3. Then we inject unpolarized current $2I$ through contact 1. The injected current will be distributed equally between the upper and lower edges in cross section A. In cross section B, however, the net current will be spin polarized due to spin mixing in probe 2. The down-spin current reaching the drain in the upper edge equals $I/2$ while the up-spin current in the lower edge is I . Therefore, the total drained current becomes spin polarized. The spin polarized current can be fed into another system (see Fig.5), where it can be detected using Hall probes 5 and 6 as discussed above.

More complicated circuits can be assembled which generate spin currents and detect them elsewhere. Note that the important principle is that as long as backscattering is not allowed, the edge current can travel long distances and the circuit is nonlocal, just as in the integer QHE [24]. In this case the current-voltage relationship is obtained by solving the circuit equations as described in Ref.[9]. The spatial scale of nonlocality is controlled by spin relaxation which can be due to spin-orbit interaction or due to magnetic impurities near graphene edge.

For simplicity, here we limit the discussion to the effects of spin-orbit. There are two main spin-orbit terms in the graphene Hamiltonian [19, 25], the so-called intrinsic and Rashba interaction, given by

$$H_{SO} = \lambda_{SO}\sigma_z\tau_z s_z, \quad H_R = \lambda_R(\sigma_x\tau_z s_y - \sigma_y s_x), \quad (23)$$

where Pauli matrices σ_i act in the sublattice space (Dirac spinor), while τ_i act in the valley space, and s_i represent physical spin. Estimates from band calculations [25] give $\lambda_R \approx 0.1$ K and a negligibly small $\lambda_{SO} \approx 6$ mK.

To estimate the backscattering rate due to the spin-orbit interaction (23), we note that for an ideal atomically sharp edge the spin-orbit would couple the left and right states with the same momentum, opening a minigap at branch crossing: $\tilde{\varepsilon} = \pm\sqrt{\varepsilon^2 + \lambda_R^2}$. However, this momentum-conserving interaction alone cannot backscatter edge states, and we need to take disorder

into account. Edges of graphite monolayers have been imaged using STM probes [13, 14], where it was found that typically edge disorder can be viewed as patches of missing atoms of characteristic size $d \sim 1$ nm. Taking into account the left-right branch mixing by spin-orbit H_R , characterized by small mixing ratio of $\lambda_R/|\varepsilon| \ll 1$ away from branch crossing, we obtain an estimate of the backscattering mean free path:

$$\ell(\varepsilon) \sim (\varepsilon/\lambda_R)^2(\ell_B/d)^2d, \quad |\varepsilon| \gtrsim \lambda_R, \quad (24)$$

which gives $\ell \sim 10$ μm for typical $\varepsilon \sim 10$ K. The factor $(\ell_B/d)^2 \gtrsim 1$ accounts for the magnetic field dependence of disorder matrix elements.

The quadratic energy dependence in (24), with spin flip rate having a sharp peak near branch crossing, suggests [9] the possibility to control backscattering using local gate. By tuning local chemical potential to and from the branch crossing, where the spin flip rate has a sharp peak, Eq.(24), we can induce or suppress backscattering in a controlled way. Spin filtering is achieved by controlling local gates on opposite sides of the Hall bar asymmetrically.

IV. EDGE AND BULK TRANSPORT AT $\nu = 0$.

Spin flip backscattering (24) can be incorporated in the edge transport model, described by coupled equations for particle density in the two spin-polarized modes:

$$\begin{aligned} \partial_t n_1 + \partial_x \varphi_1 &= \gamma(\varphi_2 - \varphi_1) \\ \partial_t n_2 - \partial_x \varphi_2 &= \gamma(\varphi_1 - \varphi_2), \quad n_i = \nu_i \varphi_i, \end{aligned} \quad (25)$$

where $\gamma^{-1} = \ell$ is the backscattering mean free path (24) taken for ε at the Fermi level, and $\nu_{1,2}$ are compressibilities of the modes. (For brevity, we use 1 and 2 instead of \uparrow and \downarrow .) In writing Eqs.(25) we implicitly assume that fast energy relaxation maintains local equilibrium of each of the modes, which is consistent with metallic temperature dependence of transport coefficients [17].

In a stationary state, Eqs.(25) have an integral $\tilde{I} = \varphi_1 - \varphi_2$ which expresses current conservation at the edge. [In this section we use the units of $e^2/h = 1$.] The general solution in the stationary current-carrying state is

$$\varphi_{1,2}(x) = \varphi_{1,2}^* - \mathcal{E}x, \quad \mathcal{E} = \gamma\tilde{I} \quad (26)$$

Taking into account that \tilde{I} is the current in one edge, we calculate the total current as

$$I = 2\tilde{I} = \frac{2}{\gamma}\mathcal{E} \quad (27)$$

To describe the longitudinal resistance in the four-terminal geometry, one must add potential drop on voltage probes [17], which gives $R = \frac{1}{2}(\gamma L + 1)$, where L is the distance between the probes. Comparing to the data

for ρ_{xx} at $\nu = 0$ we estimate [17] $\ell \approx 0.5 \mu\text{m}$. This mean free path value, which is relatively small on the scale predicted by Eq.(24), can be explained if spin flip processes are dominated by nonintrinsic effects, such as magnetic impurities localized near the edge.

It is crucial that the edge transport model (25) treats both edges of a Hall bar in an identical way, thus predicting zero Hall effect. In order to understand the observed density dependence of Hall coefficient [16, 17], which changes sign smoothly at $\nu = 0$ without exhibiting a plateau, and of ρ_{xx} which has a sharp peak at $\nu = 0$, we need to incorporate transport in the bulk in our model. In the full edge+bulk model, the density dependence of transport coefficients arises from bulk currents short-circuiting edge currents away from $\nu = 0$. This explains, as we shall now see, the Hall effect, the peak of ρ_{xx} , the resistance fluctuations near $\nu = 0$, as well as the behavior of σ_{xx} and σ_{xy} .

We describe the transport problem in the bulk by the current-field relation, separately for each spin projection:

$$\mathbf{j}_i = -\hat{\sigma}_i \nabla \psi_i, \quad \hat{\sigma}_i = \begin{pmatrix} \sigma_{xx}^{(i)} & \sigma_{xy}^{(i)} \\ -\sigma_{xy}^{(i)} & \sigma_{xx}^{(i)} \end{pmatrix}, \quad i = 1, 2,$$

where $\psi_{1,2}$ are electrochemical potentials for two spin states. We assume that the bulk conductivities $\sigma_{xx}^{(1,2)}$, as a function of density ν , are peaked at the spin-split Landau levels. For simplicity, here we ignore possible valley splitting, in which case the spin up and down Landau levels occur at $\nu = \pm 1$ around the Dirac point. As a simplest model, below we use Gaussians

$$\sigma_{xx}^{(1)}(\nu) = e^{-A(\nu-1)^2}, \quad \sigma_{xx}^{(2)}(\nu) = e^{-A(\nu+1)^2} \quad (28)$$

with the parameter A describing the width of the levels. The Hall conductivities $\sigma_{xy}^{(1,2)}$ exhibit plateaus on either side of the peak in $\sigma_{xx}^{(1,2)}$. The dependence of $\sigma_{xy}^{(1,2)}$ on ν can be modeled with the help of the semicircle relation $\sigma_{xy}^{(1,2)}(\sigma_{xy}^{(1,2)} \mp 2) + (\sigma_{xx}^{(1,2)})^2 = 0$ which often provides a good description of conventional QHE systems [26].

The condition of charge continuity, $\nabla \mathbf{j}_i = 0$, gives a 2d Laplace's equation for the potentials, $\nabla^2 \psi_i = 0$. This equation must be solved together with the boundary conditions phenomenologically describing bulk-edge coupling:

$$\mathbf{n} \cdot \mathbf{j}_i = g(\psi_i - \varphi_i) \quad (29)$$

where \mathbf{n} is a normal vector to the boundary, and $g(\psi_i - \varphi_i)$ represents the edge-bulk leakage current density.

Although a general solution of this problem can be given with the help of Fourier method, here we consider only the case when the potentials $\psi_i(\mathbf{x})$ are varying slowly on the scale of the bar width w , which will suffice for our analysis of a homogeneous current flow. In this case, linearizing $\psi_i(\mathbf{x})$ in the direction transverse to the bar,

we can write Eqs.(29) for both edges of the bar as

$$\begin{aligned} -\sigma_{xy} \partial_x \psi_i + \sigma_{xx}(\psi_{i'} - \psi_i)/w &= g(\psi_i - \varphi_i) \\ \sigma_{xy} \partial_x \psi_{i'} + \sigma_{xx}(\psi_i - \psi_{i'})/w &= g(\psi_{i'} - \varphi_{i'}), \end{aligned} \quad (30)$$

$i = 1, 2$, where the primed and unprimed quantities denote variables at opposite edges of the bar.

Equations for the edge variables φ_i are obtained by adding the bulk-edge leakage term to Eqs.(25), giving

$$\begin{aligned} \partial_x \varphi_1 &= \gamma(\varphi_2 - \varphi_1) + g(\psi_1 - \varphi_1), \\ -\partial_x \varphi_2 &= \gamma(\varphi_1 - \varphi_2) + g(\psi_2 - \varphi_2), \end{aligned} \quad (31)$$

along with a similar pair of equations for $\varphi_{1'}$, $\varphi_{2'}$ at the opposite edge.

The solution of these eight equations, describing uniform current, is of the form $\varphi_i = \varphi_i^* - \mathcal{E}x$, $\psi_i = \psi_i^* - \mathcal{E}x$, etc., with the same linear part $-\mathcal{E}x$ for all quantities. Using the algebraic structure of this linear system and the symmetry between the edges, we reduce the number of equations from eight to two. First, it is convenient to express the parameters φ_i^* through ψ_i^* using Eqs.(31), which gives

$$\begin{aligned} \varphi_1^* &= \frac{\gamma+g}{2\gamma+g} \psi_1^* + \frac{\gamma}{2\gamma+g} \psi_2^* + \frac{\mathcal{E}}{2\gamma+g} \\ \varphi_2^* &= \frac{\gamma+g}{2\gamma+g} \psi_2^* + \frac{\gamma}{2\gamma+g} \psi_1^* - \frac{\mathcal{E}}{2\gamma+g} \end{aligned} \quad (32)$$

Writing similar equations for the variables at the opposite edge to express $\varphi_{1'}$, $\varphi_{2'}$ through $\psi_{1'}$, $\psi_{2'}$, and substituting the result in Eqs.(30), we obtain four equations for ψ_i and $\psi_{i'}$ which have the form

$$\begin{aligned} -\tilde{\sigma}_{xy}^{(1)} w \mathcal{E} &= \sigma_{xx}^{(1)}(\psi_{1'}^* - \psi_1^*) + \lambda(\psi_2^* - \psi_1^*) \\ \tilde{\sigma}_{xy}^{(1)} w \mathcal{E} &= \sigma_{xx}^{(1)}(\psi_1^* - \psi_{1'}^*) + \lambda(\psi_2^* - \psi_{1'}^*) \\ -\tilde{\sigma}_{xy}^{(2)} w \mathcal{E} &= \sigma_{xx}^{(2)}(\psi_2^* - \psi_{2'}^*) + \lambda(\psi_1^* - \psi_{2'}^*) \\ \tilde{\sigma}_{xy}^{(2)} w \mathcal{E} &= \sigma_{xx}^{(2)}(\psi_2^* - \psi_{2'}^*) + \lambda(\psi_1^* - \psi_2^*) \end{aligned} \quad (33)$$

where the coefficients in this linear system are defined as

$$\tilde{\sigma}_{xy}^{(1,2)} = \sigma_{xy}^{(1,2)} \pm \frac{g}{2\gamma+g}, \quad \lambda = \frac{w\gamma g}{2\gamma+g}. \quad (34)$$

The quantities $\tilde{\sigma}_{xy}^{(1,2)}$ represent the sum of the bulk and edge contributions to Hall conductivity for each spin.

Symmetry between the edges allows to further reduce the number of independent variables. For that we add the first two equations to obtain $\psi_1^* + \psi_{1'}^* = \psi_2^* + \psi_{2'}^*$. Also we note that all potentials can be changed by the same constant that can be chosen so that the new quantities ψ_i^* and $\psi_{i'}^*$ satisfy $\psi_i^* = -\psi_{i'}^*$. After that Eqs.(33) yield

$$\begin{aligned} \tilde{\sigma}_{xy}^{(1)} w \mathcal{E} &= 2\sigma_{xx}^{(1)} \psi_1^* - \lambda(\psi_2^* - \psi_1^*) \\ \tilde{\sigma}_{xy}^{(2)} w \mathcal{E} &= 2\sigma_{xx}^{(2)} \psi_2^* - \lambda(\psi_1^* - \psi_2^*) \end{aligned} \quad (35)$$

These two equations can be solved to find $\psi_{1,2}^*$.

Now we can find the current as a sum of the edge and bulk contributions, $I = I_{\text{edge}} + I_{\text{bulk}}$, where

$$I_{\text{edge}} = \varphi_1 - \varphi_2 + \varphi_{2'} - \varphi_{1'} = 2(\varphi_1^* - \varphi_2^*)$$

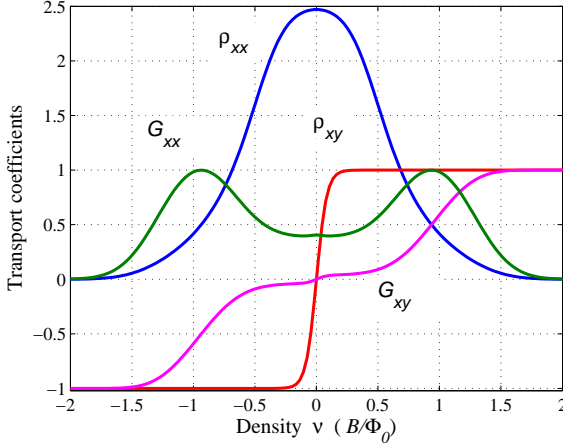


FIG. 6: Density dependence of transport coefficients $\rho_{xx} = \tilde{\gamma}w/2$, $\rho_{xy}=\tilde{\gamma}\xi/2$ and $G_{xx} = \rho_{xy}/(\rho_{xy}^2 + \rho_{xx}^2)$, $G_{xy} = \rho_{xy}/(\rho_{xy}^2 + \rho_{xx}^2)$, obtained from the edge transport model (31) augmented with bulk conductivity, Eqs.(30) (see Eqs.(36),(37) and text). Parameter values: $A = 6$, $\gamma w = 5$. Note the peak in ρ_{xx} , the smooth behavior of ρ_{xy} near $\nu = 0$, a quasi-plateau in G_{xy} , and a double-peak structure in G_{xx} .

and

$$I_{\text{bulk}} = \sigma_{xy}^{(1)}(\psi_1 - \psi_{1'}) + \sigma_{xx}^{(1)}w\mathcal{E} + \sigma_{xy}^{(2)}(\psi_2 - \psi_{2'}) + \sigma_{xx}^{(2)}w\mathcal{E}$$

After expressing φ_i through ψ_i with the help of Eqs.(32) and using the solution of Eqs.(35), we obtain a relation $I = 2\mathcal{E}/\tilde{\gamma}$, where

$$\frac{2}{\tilde{\gamma}} = \frac{4}{2\gamma + g} + \frac{w}{\rho_{xx}^{(1)}} + \frac{w}{\rho_{xx}^{(2)}} - \frac{\lambda w \left(\tilde{\sigma}_{xy}^{(1)}/\sigma_{xx}^{(1)} - \tilde{\sigma}_{xy}^{(2)}/\sigma_{xx}^{(2)} \right)^2}{2 + \lambda/\sigma_{xx}^{(1)} + \lambda/\sigma_{xx}^{(2)}}. \quad (36)$$

The quantities $\rho_{xx}^{(1,2)}$ are defined as $\rho_{xx}^{(i)} = \sigma_{xx}^{(i)}/(\tilde{\sigma}_{xy}^{(i)2} + \sigma_{xx}^{(i)2})$. The quantity $\tilde{\gamma}$, Eq.(36), replaces γ in Eq.(27). In the absence of bulk conductivity, $\sigma_{xx}^{(1,2)} \rightarrow 0$, we recover the result for pure edge transport, $\tilde{\gamma} = \gamma$.

The Hall voltage can be calculated from this solution as $V_H = \frac{1}{2}(\varphi_1 + \varphi_2 - \varphi_{1'} - \varphi_{2'})$, where φ_i , $\varphi_{i'}$ are variables at opposite edges. We obtain $V_H = \xi\mathcal{E}$, where

$$\xi = 2w \frac{\tilde{\sigma}_{xy}^{(1)} \left(\lambda + \sigma_{xx}^{(2)} \right) + \tilde{\sigma}_{xy}^{(2)} \left(\lambda + \sigma_{xx}^{(1)} \right)}{2\sigma_{xx}^{(1)}\sigma_{xx}^{(2)} + \lambda\sigma_{xx}^{(2)} + \lambda\sigma_{xx}^{(1)}}. \quad (37)$$

This quantity vanishes at $\nu = 0$, since $\sigma_{xy}^{(1)} = -\sigma_{xy}^{(2)}$ and $\sigma_{xx}^{(1)} = \sigma_{xx}^{(2)}$ at this point due to particle-hole symmetry.

Transport coefficients, obtained from this model for typical parameter values, are displayed in Fig.6 which reproduces many of the key features of the data (see Fig.1 in Ref.[17]). In particular, the peak in ρ_{xx} is due to edge transport near $\nu = 0$. The suppression of ρ_{xx} at finite ν is due to the bulk conductivity short-circuiting the edge transport. The bulk and edge contributions to transport

can be discerned from the double peak structure in G_{xx} in Fig.6. The peaks correspond to the bulk Landau level contributions, Eq.(28), whereas the part of G_{xx} between the peaks, exceeding the superposition of two Gaussians, Eq.(28), is the edge contribution. The Hall resistance ρ_{xy} is nonzero due to imbalance in $\sigma_{xy}^{(1,2)}$ for opposite spin polarizations away from $\nu = 0$. Interestingly, ρ_{xy} in Fig.6 exhibits no plateau, while G_{xy} calculated from ρ_{xy} and ρ_{xx} displays an under-developed plateau-like feature. Overall, this behavior resembles that of the experimentally measured transport coefficients [16, 17].

Another notable feature of the measured ρ_{xy} and ρ_{xx} is enhanced fluctuations near zero ν . These fluctuations are found to be strong in Ref.[16], where ρ_{xy} changes sign several times near $\nu = 0$. They are also present, although are not as dramatic, in Ref.[17]. In the latter case, both ρ_{xy} and ρ_{xx} exhibit noisy behavior in the interval near $\nu = 0$ comparable to the ρ_{xx} peak width. As Ref.[17] points out, this behavior is consistent with the edge transport model. In the absence of bulk transport, the distribution of potential along the edge depends on the local backscattering rate $\gamma(x)$, whereby Eq.(26) is replaced by

$$\varphi_{1,2}(x) = \varphi_{1,2}(0) - \tilde{I} \int_0^x \gamma(x') dx'.$$

Fluctuations of γ arise due to its sensitivity to the local value of Fermi energy in the spin-orbit scattering model, Eq.(24), and, similarly, for the magnetic impurity scattering mechanism. Assuming that the random part of γ is of a white noise character, we obtain strong fluctuations $\delta\varphi_{1,2}(x)$ along the edge of magnitude that scales as a square root of the edge length. These fluctuations will contribute equally to the longitudinal and transverse voltage, since they are uncorrelated on the opposite sides of the Hall bar. The absence of fluctuations away from $\nu = 0$ can be understood as a result of bulk conductivity short-circuiting the edge current, which will equilibrate potentials on the opposite sides of the Hall bar.

The above discussion summarizes the results drawn from an attempt to model quantum Hall transport in graphene at $\nu = 0$ by counter-circulating edge states. By taking into account backscattering within one edge as well as conduction in the bulk which short-circuits edge transport away from the neutrality point, this model accounts for the observed behavior of transport coefficients. Still, since no direct evidence for spin polarization has yet been found, more experimental and theoretical work will be needed to confirm the chiral spin-polarized edge picture of the $\nu = 0$ state. If proven to exist in graphene, these states will provide a unique setting to study spin transport as well as other interesting phenomena.

This work is supported by NSF MRSEC Program (DMR 02132802), NSF-NIRT DMR-0304019 (DA, LL), and NSF grant DMR-0517222 (PAL).

-
- [1] K. S. Novoselov *et al.*, Science, **306**, 666 (2004); Proc. Natl. Acad. Sci. USA, **102**, 10451 (2005).
- [2] K. S. Novoselov *et al.*, Nature **438**, 197 (2005);
- [3] Y. Zhang, Y.-W. Tan, H. L. Stormer and P. Kim, Nature **438**, 201 (2005).
- [4] V. P. Gusynin and S. G. Sharapov, Phys. Rev. Lett. **95**, 146801 (2005).
- [5] K. S. Novoselov *et al.*, Nature Physics **2**, 177 (2006).
- [6] K. S. Novoselov *et al.*, Science 315, 1379 (2007).
- [7] B. I. Halperin, Phys. Rev. B**25**, 2185 (1982).
- [8] N. M. R. Peres, F. Guinea, A. H. Castro Neto, Phys. Rev. B**73**, 125411 (2006).
- [9] D. A. Abanin, P. A. Lee and L. S. Levitov, Phys. Rev. Lett. **96**, 176803 (2006).
- [10] L. Brey and H. A. Fertig, Phys. Rev. B**73**, 195408 (2006)
- [11] T. Matsui *et al.*, Phys. Rev. Lett. **94**, 226403 (2005)
- [12] Y. Niimi *et al.*, Phys. Rev. Lett. **97**, 236804 (2006)
- [13] Y. Kobayashi *et al.*, Phys. Rev. B **71**, 193406 (2005).
- [14] Y. Niimi *et al.*, Phys. Rev. B **73**, 085421 (2006).
- [15] H. A. Fertig and L. Brey, Phys. Rev. Lett. **97**, 116805 (2006).
- [16] Y. Zhang *et al.*, Phys. Rev. Lett., **96**, 136806 (2006).
- [17] D. A. Abanin *et al.*, Phys. Rev. Lett. **98**, 196806 (2007).
- [18] B. A. Volkov and O. A. Pankratov, Pis'ma Zh. Eksp. Teor. Fiz. **42**, 145 (1985) [Engl. transl. JETP Lett. **42**, 178 (1985)]; review in: O. A. Pankratov, Semicond. Sci. Technol. **5**, S204-S209 (1990).
- [19] C. L. Kane and E. J. Mele, Phys. Rev. Lett. **95**, 226801 (2005).
- [20] B. A. Bernevig, T. Hughes, S.-C. Zhang, Science **314**, 1757 (2006).
- [21] D. P. DiVincenzo and E. J. Mele, Phys. Rev. B **29**, 1685 (1984).
- [22] L. Fu, C. L. Kane, cond-mat/0606336, unpublished.
- [23] M. Fujita, K. Wakabayashi, K. Nakada, and K. Kusakabe, J. Phys. Soc. Jpn. **65**, 1920 (1996).
- [24] M. Büttiker, Phys. Rev. B **38**, 9375 (1988).
- [25] H. Min *et al.*, Phys. Rev. B**74**, 165310 (2006).
- [26] A. M. Dykhne and I. M. Ruzin, Phys. Rev. B**50**, 2369 (1994); S. S. Murzin, M. Weiss, A. G. Jansen, and K. Eberl, Phys. Rev. B**66**, 233314 (2002)
- [27] M. O. Goerbig, R. Moessner, B. Doucot, Phys. Rev. B**74** 161407 (2006)
- [28] D. A. Abanin, P. A. Lee, and L. S. Levitov, Phys. Rev. Lett. **98**, 156801 (2007).